Nuclear Inst. and Methods in Physics Research, A 1035 (2022) 166807

Contents lists available at ScienceDirect

Nuclear Inst. and Methods in Physics Research, A

journal homepage: www.elsevier.com/locate/nima

Spectroscopic autoradiography of alpha particles using a parallel ionization multiplier gaseous detector

Hugo Lefeuvre [a,b,*], Jérôme Donnard [c], Michael Descostes [d,e], Sophie Billon [b], Samuel Duval [c], Tugdual Oger [c], Hervé Toubon [d], Paul Sardini [b]

[a] ERM (SARL), 7 rue Albert Turpain, 86000, Poitiers, France
[b] IC2MP – HydrASA, Poitiers University UMR 7285 CNRS, France
[c] AI4R (SAS), 2 rue Alfred Kastler, Nantes, France
[d] ORANO Mining, R&D Dpt, 125 Av. de Paris, 92320 Châtillon, Paris, France
[e] Centre de Géosciences, MINES ParisTech, PSL University, 77300 Fontainebleau, France

ARTICLE INFO

Keywords:
Alpha particles
Digital autoradiography
Alpha spectroscopy
Uranium decay products
Mining activities
Parallel ionization multiplier

ABSTRACT

Geoscience is a field of study where nuclear instruments find their place for conducting specific measurements of radioactivity, usually to improve the monitoring of natural processes using naturally-occurring radioactive tracers, but also for the nuclear industry linked to the mining sector. In geological samples, the location and identification of the minerals bearing radioactivity at the thin-section scale remains a major challenge as the detection limit of the usual elementary microprobe techniques is far higher than the concentration of most of the natural radioactive decay products. The location of each decay product, as in the case of uranium-238 series in a geomaterial is interesting for relating radionuclide concentrations to mineralogy. The present study aims to provide spectroscopic autoradiography analysis method for measuring the initial energy of alpha particles with a parallel ionization multiplier gaseous detector. This spectroscopic autoradiography method was successfully used to reproduce the alpha spectra from a ^{238}U decay chain on a geological sample at the thin-section scale. The characteristics of this measurement are an energy spectrum resolution of 17.2% (FWHM) at 4647 keV and a spatial resolution of at least 50 μm. Even if the efficiency of energy spectrum reconstruction is low (4.4%) compared to the efficiency of a simple autoradiograph (50%), this novel measurement approach offers the opportunity to select areas on an autoradiograph to perform an energy spectrum analysis within that area. This opens up possibilities for the detailed analysis of heterogeneous geological samples containing natural alpha emitters such as uranium-238 and radium-226.

1. Introduction

Autoradiography [1] is a non-destructive imaging method for studying and locating in two dimensions the radioactivity emanating from a surface sample, at scales ranging from hectometer to micrometer [2]. The distinctiveness of autoradiography is based on the fact that the source is the object itself. Radioactivity imaging is performed using a detector which integrates and spatializes the radioactive emissions during a given acquisition time. The image definition is closely related to the choice of sensor. Film autoradiography (FA) using a silver-bromide emulsion was the first technique employed [3]. It is still widely used because of its low cost and very good spatial resolution (about 10 μm). To reveal the signal information, the film must be digitized. Advances in autoradiograph technology now makes it possible both to digitize the activity map directly and to observe the signal accumulation in real time. Autoradiography is well suited for use in the life and earth sciences. Thin sections of radiolabelled animal organs mounted on microscope glass slides are conventionally imaged by autoradiography. *Ex vivo* autoradiography is used by biologists as a complementary tool in positron emission tomography (PET) [4,5], for instance to better understand drug effects or degenerative diseases. Applications of autoradiography for geosciences include, among others, the characterization of pore space and transport properties of rocks [6,7,8], and the distribution of natural disintegration series in rocks [9].

In that context, the study of autoradiography use for alpha particle characterization is increasing in the geosciences. The present contribution is focused on the study of the natural series found in geo-materials (rocks or U mill tailings). A lot of devices have been developed for imaging the emission of alpha particles. The traditional method uses a solid-state nuclear track detector (SSNTD). SSNTD is a medium, typically a polycarbonate film, in which the passage of an ionizing particle leaves a latent track that can be made visible by an appropriate chemical treatment. Depending on the track size, the observation can

* Correspondence to: IC2MP - UMR 7285, B27, 4 RUE MICHEL BRUNET, TSA 51106, 86073 POITIERS, Cedex 9, France.
E-mail address: hugo.lefeuvre@univ-poitiers.fr (H. Lefeuvre).

https://doi.org/10.1016/j.nima.2022.166807
Received 16 February 2022; Received in revised form 21 April 2022; Accepted 25 April 2022
Available online 6 May 2022

be performed with the naked eye, using an optical microscope or a scanning electron microscope (SEM). For further details the reader can refer to applications in geosciences [10,11,12] and also in biology [13]. Phosphor screens autoradiography (PSA) is an alternative method using reusable films, that used to be employed for imaging the ppm of U and Th in geo-materials [14]. The detection of particles is based on the property of phosphorescence. The energy imparted by incident radiation (light, X-rays, gamma rays, alpha or beta particles) is temporarily stored by the excited atoms in a photostimulable phosphor plate based on BaFBr: Eu^{2+}. Then, de-excitation can be induced by laser scanning to stimulate characteristic emissions of photons that are interpreted to form an image. All autoradiograph techniques of alpha particles described above store information in films. The sample exposure time can only be estimated, so there is a high risk of overexposure or underexposure. Nowadays, real-time autoradiography is becoming increasingly favoured. The advantages of this approach are the direct counting of the emissions, the direct digitization of the image in a raster file, and the real-time acquisition. The first application of real-time autoradiographs was in the field of medicine. The "α-Camera", used in alpha-therapy, was developed using a scintillator and a CCD camera [15,16] with detector area about 5×5 cm^2. The iQID system [17], which uses a similar technology to the α-Camera, is described in [18]; the detector area can be 4 cm or 12.5 cm diameter. This device has applications in preclinical and clinical scintigraphy [19]. For radiotherapy, the Timepix chip based on a pixelized semi-conductor is used for alpha particle autoradiography with 14×14 mm^2 area [20,21]. First developed for biological applications such as alpha-therapy (using ^{223}Ra) [22,23], the BeaQuant system also created the first alpha autoradiograph of a geological thin section [24]. This technology is based on a gaseous detector incorporating micromesh Parallel Ionization Multiplier (PIM) [25,26,27] which allows the detection of both alpha and beta particles, together or separately. Alpha autoradiography using this detector is considered to be not disturbed by beta particles when used in the alpha imaging mode. The special feature of this autoradiograph is its large detection surface (up to 20×20 cm^2) in comparison with other real-time autoradiograph. It has a good spatial resolution (<50 μm for alpha and 20 μm for beta particles, mainly because the charge distribution is different), and is insensitive to X-ray and gamma. The linearity of the detector reaches five orders of magnitude. The maximal acceptable counting rate over the whole analysed area is 20×10^3 cps (counts per second), and the background level for alpha counting is in the order of 6.3×10^{-4} cps/mm^2. The efficiency for alpha particle detection is 50% according to Billon, et al. 2019 [28].

Concurrently, spectroscopic autoradiography (called SA) is performed by simultaneously combining autoradiography with a spectral measurement. For alpha particles, different types of detector technologies make this dual measurement possible. But there is often a trade-off between spatial resolution, energy resolution and the field of view.

SSNTD can be used as a basic SA, by analysing the size distribution of the alpha tracks [29,30]. A previous study employing SSNTD demonstrated an energy resolution optimized at around 2% FWHM [31] by using the range property of alpha particles. The application is however limited when alpha tracks are overlaid on each other, if the activity is too high or if the exposure time is too long.

A scintillator coupled to a silicon photomultiplier array allows the measurement of the particles' energy and emission point. For instance, in [32], the plutonium found around Fukushima has been studied by spectroscopy allowing the separation of alpha and beta particles. The energy resolution was good, but the spatial resolution (of 600 μm FWHM) was not suitable for high resolution autoradiography applications because of the limited pixelisation (64 channels over a 26×26 mm^2 detection area).

As an alternative to SiPM, a demonstration using an organic scintillator (stilbene) coupled to a 8×8 position-sensitive photomultiplier tube (PS-PMT) [33] gave an energy resolution of 21.6% FWHM for ^{241}Am.

Using Timepix [34] for counting and the alpha spectrometer modes to identify and quantify radon and thorium gave an energy resolution of 2.3% for ^{241}Am (α-decay energies are 5.486 MeV). Following further calibration in the alpha mode, the energy resolution is 0.7% FWHM [35,36]. However, in terms of imaging, the restricted detection area of 14×14 mm^2 makes the use of this method impractical for large samples. The spatial resolution can reach 18 μm [37] for alpha particles.

According to [38], the iQID device can locate and determine the energy of individual particles, with sufficient energy resolution to distinguish between different particle types (fission fragment, β, and α decay). However, using a ZnS(Ag) scintillator the expected energy resolution would not be better than 40% FWHM at 5.5 MeV according to Refs. [39,40].

The radiobiology application of the fluorescent nuclear track detector (FNTD) has demonstrated its ability to visualize individual alpha particles and simultaneously measure their position, trajectory direction and energy with good accuracy [41]. However, the detection area is limited (100×100 μm^2) and the energy resolution is 11.8% FWHM for an ^{241}Am source according to [42].

In the field of gaseous detectors, despite the possibility of having a good energy resolution [43,44], there are few instruments that can combine imaging and energy measurement. For example, a 31 cm thick time projection chamber using CF_4 showed an energy resolution of 6.7% ($K = 1$) at 5.3 MeV, and a spatial resolution of 6.8 mm [45]. The latter detector has been used to measure radioactive impurities of ^{238}U and ^{232}Th in low activity samples. The resolutions of different technologies are summarized in Table 1.

In order to meet the needs of the analysis of radioactive geological samples (pluri-centimetric sample and good spatial resolution), this study examines the possibility of combining the spatial and energy measurement of emitted alpha particles using the BeaQuant system. Our objective is to evaluate the possibility of obtaining the energy spectrum of alpha particles, with the final aim of spatializing the energy distribution on the autoradiograph. This, in order to better characterize the distribution of natural decay products (notably the ^{238}U series) that can be found in geomaterials [46,47,48]. Examples for ^{238}U series are provided.

2. Alpha SA method using a parallel ionization multiplier

Originally, the used detector was developed and optimized for beta particle autoradiography [25]. Because alpha and beta particles do not interact in the same way with the detector, a simulation model was performed with the Geant4 toolkit in order to understand and interpret the data measured. Alphas deposit more energy than betas per unit path length and have a quasi-straight trajectory. Knowledge of the particles' position and energy along their trajectory through the detector is crucial for developing a spectroscopy method.

2.1. Sample material and the PIM detector characteristics

2.1.1. Characteristics of a geological sample emission spectrum

Determining the alpha emission energy spectra using the PIM is our main goal. Let E_0 be the emission energy of an alpha particle when leaving the source/sample and penetrating the gas medium. E_0 is influenced by the self-absorption and the loss of energy in interaction with the source media before the arrival in the detector gas media. Then, the emission energy spectrum of alphas can be modified by the source geometry (thickness) and nature (density). Three examples of spectra obtained with the AASI simulation program [49] are shown in Supplementary Material, Figure S1. Note that a source is named as "thin source" if its thickness can be neglected with respect to the mean range of the alpha particles propagating into it, and "thick source" otherwise. The red spectrum corresponds to a 0.018 μm (9 g/cm^3) 5485 keV mono-energetic ^{241}Am alpha source. The blue one corresponds to the same emitter but in a 9 μm (9 g/cm^3) thick source characterized

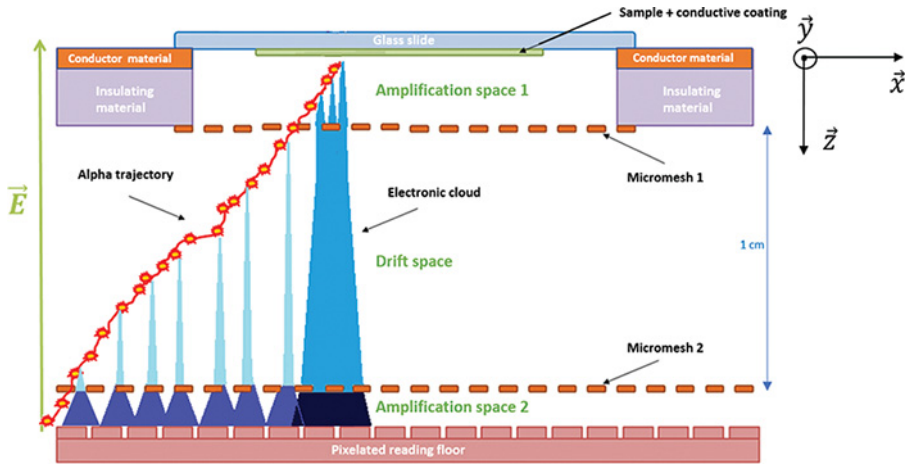

Fig. 1. Principle of the PIM detector. An alpha particle is coming from the sample, and interacts with the gas within the chamber of the detector.

Table 1
Comparative table of important parameters describing the spectroscopic autoradiography devices. These parameters are related to alpha particles detection.

Detector	Sensitive material technology	Energy resolution (FWHM)	Spatial resolution	Active area	Reference(s)
SiPM	Ce:GAGG Scintillator	13% (5.5 MeV)	600 μm	26 × 26 mm^2	[32]
PSPMT	Stilbene	21.6% (5.5 MeV)	–	20 × 20 mm^2	[33]
CCD Camera	ZnS(Ag)	56.4% (5.5 MeV)	390 μm	26 × 26 mm^2	[40]
Timepix	Silicon semiconductor	0.73% (5.5 MeV)	18 μm	14 × 14 mm^2	[36,37]
SSNTD	Lexan polycarbonate	6.9% (5.2 MeV)	Several micrometers		[29,30]
FNTD	Al_2O_3:C,Mg crystals	11.8% (5.49 MeV)	–	70 × 70 μm^2	[42]
Micro-TPC	Gas: CF_4	15.8% (5.3 MeV)	6.8 mm	95 × 95 mm^2	[45]
Coplanar electrode	Gas: Xe + 0.7% CH_4	1.3% (5.49 MeV)	No position	100 mm	[43]
Coplanar electrode	Gas: Ar + 10% CH_4	2.2% (5.49 MeV)	No position	–	[44]

by a staircase shape falling at 5485 keV. The third spectrum (in green), resulting from a multi-alpha 9 μm thick source (9 g/cm^3, the same as the blue spectrum), illustrates the case of a "real" geological sample containing the 8 alpha emitters isotopes from the decay chain of ^{238}U at secular equilibrium. One can appreciate the complexity of the spectroscopic approach applied to geological samples. Indeed, they are often in the form of materials of about 30 μm thick on a thin section, and may exhibit the three natural decay chains (^{238}U, ^{235}U and ^{232}Th) in which the most energetic alphas emitting from ^{214}Po (7686 keV) have an average internal range of 20 to 40 μm. This range combined with usual thickness of the sample means that there is considerable self-absorption and energy loss.

2.1.2. PIM detector description and charge readout

The detector structure used for this study is schematized in Fig. 1. The active part of the detector is a volume of gas segmented into three zones by two thin micromeshes that are sandwiched between a cathode and an anode. The cathode of the detector is the sample itself, which is mounted on a microscope slide and preferably coated with a conducting layer. The gap of 400 μm between the sample and the first micromesh is achieved with a spacer machined with FR-4 material. This gap creates the first amplification space (of gain G_1), placed directly in contact with the sample. The second zone of 1 cm thickness is a drift space used to propagate the electron cloud. It is defined by the space between the two micromeshes. Finally, the space between the second micromesh and the segmented anode defines the third zone, which is a second amplification stage (of gain G_2).

An alpha particle coming from the sample interacts with the gas and generates electron-ion pairs by ionization of the gas atoms along its rectilinear-like path. The number of primary electrons ($nb_{primary\_charge}$) is proportional to the raw energy deposited (E_{dep}) by the alpha particle in the detector. The electrons created will be multiplied and collected on the segmented reading anode. The induced currents generated by the charge drift in the amplification space 2 are measured by application-specific integrated circuits (ASICs).

The intensity of the signal measured is more intense at the position where the alpha particles first ionize the gas (black colour in amplification space 2, Fig. 1), than the intensity measured from the interactions in the drift space (dark blue in amplification space 2). The two histograms representing the charge of the collected electrons (called "charge histograms") are recorded for each event along the X and Y axes. The initial position of the alpha particles, the energy deposited in the detector and the projected X and Y distances of the trace are estimated thanks to these charge histograms. Unlike calorimeters, since not all particles stop in the gas, the deposited energy is not directly proportional to the emission energy E_0.

2.2. Simulation of the alpha emission interaction in PIM with Geant4

2.2.1. Behavior of alpha particles interacting with the detector

The PIM detector and the alpha tracks modelled with Geant4 are shown in Fig. 2. For instructive purposes a point-like source having energies (E_0) uniformly distributed between 0 and 8 MeV has been simulated. One can clearly notice that alpha particles show a probability of interacting with micromesh 1. The latter plays an important role because its geometry allows only a certain range of incidence angle of alpha paths. The parameters of micromesh 1 are the diameter of the grid wire (18 μm), the distance between the axes of two adjacent wires (45 μm) and the material (stainless steel). The angle of incidence θ is the angle defined by the particle trajectory and the normal to the gas-sample interface. The cut-off angle θ_{max} of the simulated micromesh has been estimated to 68°. The depth of the gas passed through (Z coordinate) as a function of the emission energy E_0 of the alpha particle is displayed in Fig. 3.

From the calculated 2D histogram (Fig. 3, left), three types of alpha particle behaviour can be distinguished with respect to the detector.

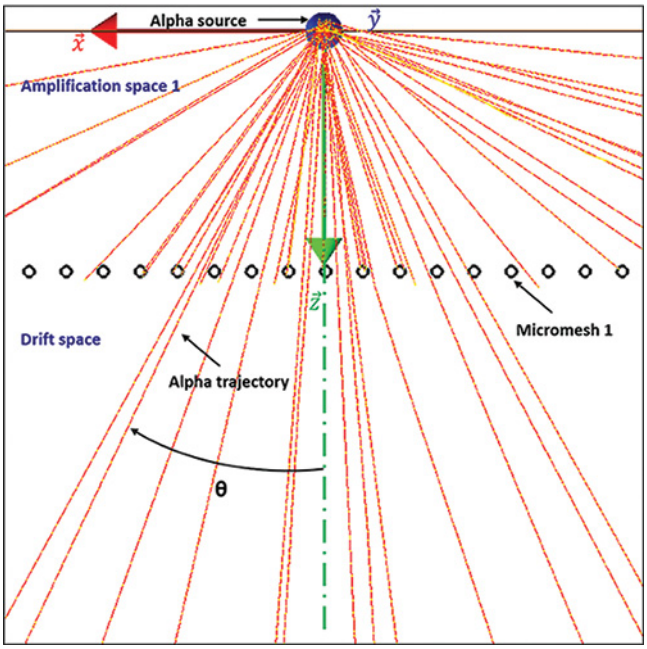

Fig. 2. Alpha track visualization with Geant4 in the (X, Z) plane close to micromesh 1. The alpha source is a point source. Micromesh 1 is simulated by a set of bars parallel to the X and Y axes, the bars parallel to the Y axis in the (X, Y) plane are visible. The z distance between the source and micromesh 1 is 400 μm.

- *Type-1: Alphas that do not pass through micromesh 1.* If $E_0 < 40$ keV, the alpha range in the gas is less than the depth of the first amplification space (400 μm); this explains why particles with low emission energy never pass through micromesh 1. If E_0 ranges from 40 keV to 6 MeV, about 85% particles do not pass through micromesh 1. From 6 MeV onwards, this proportion decreases progressively to about 63% for $E_0 = 8$ MeV. If $E_0 > 40$ keV, an alpha particle deposits part of its energy in the first amplification space and may or may not be stopped by micromesh 1. For example, when an alpha particle is emitted with an angle of incidence $\theta > \theta_{max}$, then it is always stopped by micromesh 1. Note that the probability of an alpha particle passing through micromesh 1 increases slightly with E_0. Finally, it is deduced that it is difficult to exploit type-1 alphas for spectroscopic measurements, as the energy deposition in the gas is not sufficient due to the small depth of the first amplification space. The fact that these alphas represent on average 80% of the total count is a factor limiting the efficiency of the spectroscopic measurement.
- *Type-2*: *Calorimetric alphas.* These alphas pass through micromesh 1, but do not reach micromesh 2. The deposited energy of type-2 alphas is equal to the emission energy. For 40 keV $< E_0 <$ 1 MeV, the particles passing through micromesh 1 are totally calorimetrized in the gas, i.e., none of them ever reach micromesh 2. For 1 MeV $< E_0 <$ 2.7 MeV, the proportion of calorimetrized alpha particles gradually decreases until it becomes zero. For $E_0 > 2.7$ MeV, the proportion of calorimetric alpha particles is generally low. This effect is due to the cut-off angle which imposes a maximum range in the gas (and consequently a maximum energy of 2.7 MeV for which a particle cannot be stopped in the gas after passing through micromesh 1). Nevertheless, this proportion tends to increase to about 10% for E_0=8 MeV. This increase for high E_0 can be explained by the fact that at high energies, alpha particles that interact with micromesh 1 can continue their path to be calorimetrized. These events will be considered as "polluting events" for the proposed application. The type-2 alphas represent on average only 5% of the alphas emitted by the simulated uniform source. The fact that these alphas were not used for the spectroscopy is explained below in more detail.
- *Type-3: through-going alpha.* These are the alpha particles that have managed to pass through the entire depth of the gas and end up in the anode of the detector (at the $Z = 1$ cm coordinate). The energy deposited is therefore different from the initial energy. They represent on average 15% of the events recorded. On the green curve, the proportion of the crossing particles is constant and around 20% from 2.7 MeV. Around 6 MeV, there is a theoretical increase in the proportion of the particles passing through with energy. These alphas will be highlighted below because they exhibit a link between E_0 and the deposited energy.

2.2.2. From deposited energy to emission energy

To exploit the energy deposited by the crossing particles, the length d of the alpha track will be used:-

$$d = \sqrt{x^2 + y^2 + z^2} \text{ (cm)} \quad (1)$$

where x and y are the projected distances along the X and Y axes respectively, and z the thickness of the gas passed through along the Z axis. However, z is an unknown for type-2 alphas because the detector does not allow us to measure this coordinate: it is not a time projection chamber. This explains why type-2 alphas are not used for spectroscopy. Nevertheless, for type-3 alphas, it is possible to fix z to the thickness of the detector (1 cm).

Knowing the deposited energy E_{dep} and the length of the track d, it is possible to relate E_{dep}/d to the emission energy of the alpha particle E_0. For this, Monte Carlo simulation was used to determine the distribution E_{dep}/d as a function of E_0 for all alpha particles types (Fig. 4).

The three types of alpha events described above can be observed in Fig. 4, being indicated by three zones of visible colour on the right-hand distribution. Firstly, the area bordered in green corresponds to the alphas that pass completely through the detector (type-3). For these alphas, the function $E_{dep}/d = f(E_0)$ follows a bijection. The result is equivalent to the averaged Bethe curve. Secondly, the area bordered in red corresponds to the calorimetrized alphas (type-2). These alphas disrupt the expected bijective contribution between 1 MeV and 3 MeV. Thirdly, the alpha events in the orange-bordered area are those that do not pass through micromesh 1 (type-1). The length d is greatly overestimated which induces $E_{dep}/d < 200$ keV/cm for most of these events. Only those alphas that contribute to the bijective distribution (type-3 alpha - selection in green) are selected; calorimetrized alphas (type-2) cannot be considered for the analysis because they fall outside the bijective zone. Moreover, the type-2 alpha has initial energy E_0 directly proportional to E_{dep}. But type-2 alpha cannot be used for energy measurement above 2.7 MeV because their proportion is close to zero (except for "polluting events"). For application to the ^{238}U series, the measurement range needs to be up to 8 MeV. The way of selecting type-3 alphas is detailed in the next section.

2.3. Analysis method for spectral reconstruction

According to the simulation, it has been shown that among the three types of events generated, only type-3 alphas can be used for reconstructing the energy spectrum (from 3 MeV to 8 MeV). The low threshold of 3 MeV will be further explained in Section 2.3.4. Only the alphas passing through the detector can be used for a spectral reconstruction beyond 3 MeV, because in this case the length (d) of the track is known and the deposited energy tends to avoid the Bragg peak at the end of the path. This section describes the method for measuring the energy (E_0) spectrum of an alpha-emitting source using the charge histograms.

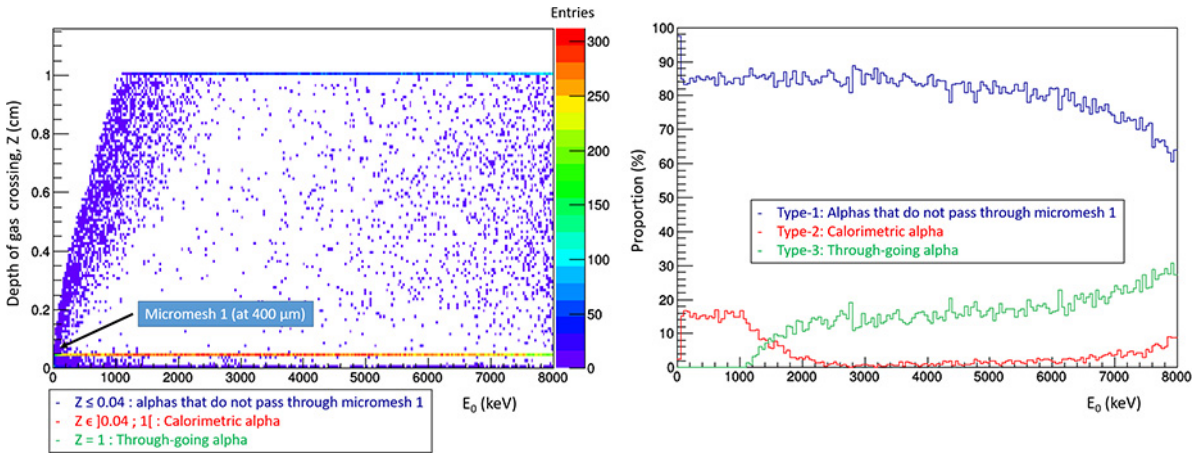

Fig. 3. Left: 2D histogram showing the depth of gas passed (Z in cm) as function of the alpha emission energy E_0. Right: Proportion of the three identifiable alpha event types as a function of E_0.

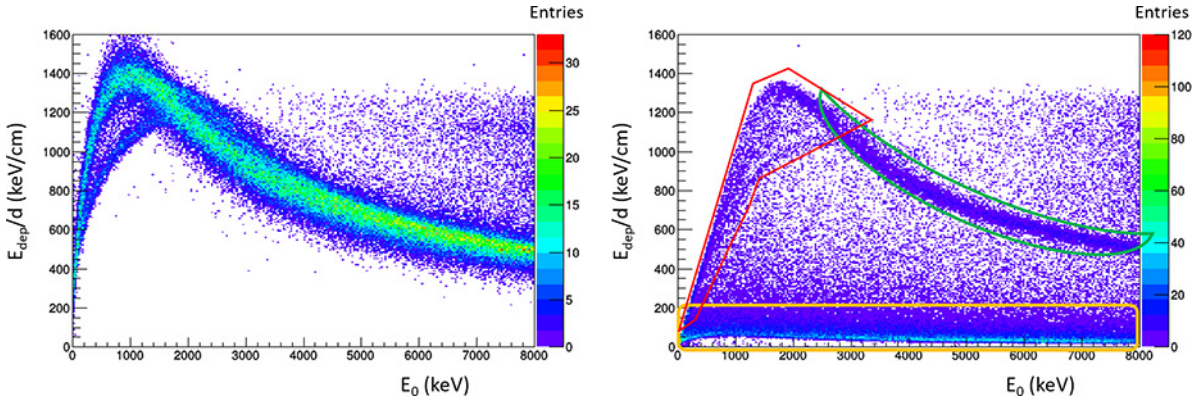

Fig. 4. Bethe curves ($E_{dep}/d = f(E_0)$) obtained using Geant4 simulations, for all types of alphas. Left: using $d = \sqrt{x^2 + y^2 + z^2}$, which cannot be experimentally measured; Right: using $d = \sqrt{x^2 + y^2 + 1}$ which can be estimated using the PIM. The orange, red and green selections correspond to alpha types 1, 2 and 3, respectively.

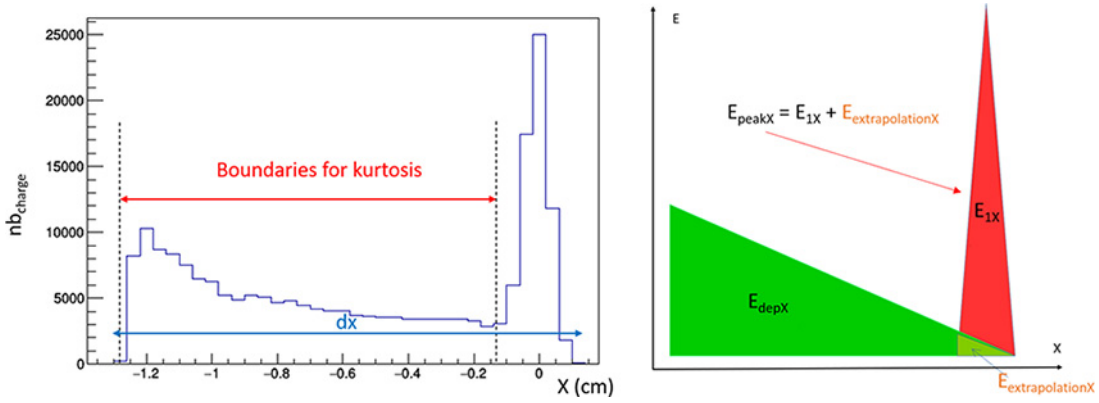

Fig. 5. Left: Boundaries used in charge histogram (in X here) for the calculation of kurtosis (for type-2 alpha event example). Right: schematic illustration of the total energy calculation.

2.3.1. Particle identification

The question is now to find a criterion to select type-3 alphas only. The statistical criterion used is kurtosis, calculated on the charge histograms collected on the anode. The kurtosis coefficient can be interpreted as a "shape feature" for charge histograms: a high value of kurtosis indicates that the distribution is rather concentrated; in contrast, a low value of kurtosis describes a flat distribution. Normalized kurtosis was used for the calculation (see Eq. (3)). It is −1.2 for a continuous uniform distribution, and rises to +3 for a Laplace distribution. It is 0 for a normal distribution. This coefficient is useful because in most of the cases, the traversing alpha (type-3) does not deposit the "Bragg peak" at the end of the path: it presents a flatter profile than the calorimetric alpha (type-2) ones. But in a few cases, the peaked characteristic of the Bragg curve can be present in charge histograms for type-3 alpha. Moreover, calorimetric alpha can have a charge distribution close to flat. Such a wide range of behaviour makes it difficult to show a perfect discrimination between type-2 and type-3 alpha. Fig. 5 (on the left) gives an example of a charge histogram. The amplification "peak" is located here at position $X = 0$ cm while the

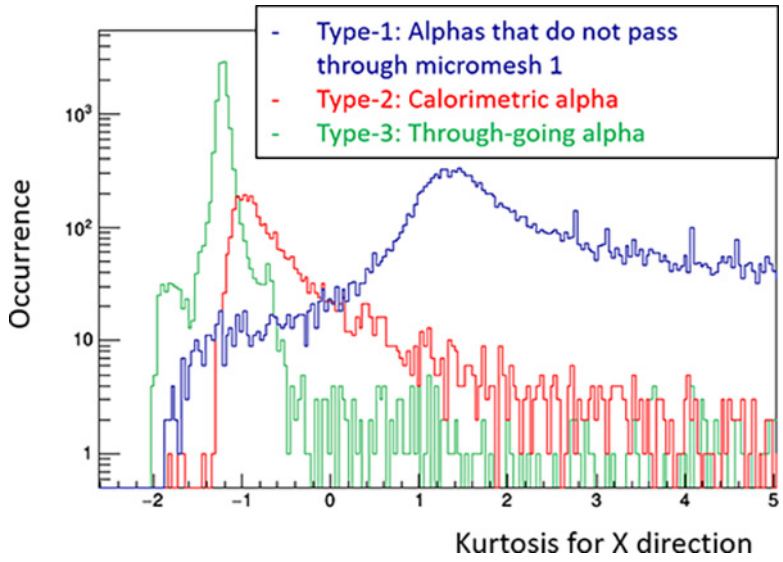

Fig. 6. Kurtosis distribution for the three alpha types; type-1 in blue; type-2 in red; type-3 in green.

"Bragg peak" is located at $X = -1.2$ cm. This is why it is necessary to ignore the amplification peak for the calculation of kurtosis.

If X is a real random variable defined on an interval, then the kurtosis of X, Kurt(X), is defined such as:-

$$Kurt\,[X] = E\left[\left(\frac{X-\mu}{\sigma}\right)^4\right] = \frac{\mu_4}{\sigma^4} \tag{2}$$

and the normalized kurtosis is:-

$$KurtNorm[X] = Kurt[X] - 3 \tag{3}$$

where E is the mathematical expectation; μ = E(X), the average of X; μ_4 is the central moment of order 4; and σ, the standard deviation. Kurtosis is calculated bin by bin on the charge histograms. Fig. 6 shows the kurtosis distribution for the three types of alpha particles. The kurtosis of the type-3 alphas shows a different distribution; for example, the majority of the type-3 alphas have a kurtosis close to −1.2 (green distribution, Fig. 6) while type-1 and type-2 alphas exhibit a kurtosis above −1.

By selecting the peak related to the type-3 alphas, most of the alpha which are not usable for spectroscopic measurement is eliminated. The upper boundary of the peak selection is at the interface between the "pass-through" particles (green) and the calorimetrized particles (red). This interface is not clearly defined as an overlap occurs between the green and red curves. However, by placing the threshold at the intersection, on the abscissa there is a low percentage (3.4%) of calorimetrized particles selected (against 95.8% of pass-through alpha selected, and 0.8% of alpha that do not pass through micromesh 1). The setting of this threshold was optimized to reduce this percentage but without lowering the final efficiency. An identical kurtosis calculation was also performed on the Y charge histogram. Considering the charge histograms according to X and Y and using kurt(X) < −1.1 && kurt(Y) < −1.1, 6.4% of the events were selected from all the detected alphas used for autoradiography analysis. Once the (−1.1) threshold is defined, it is a constant that does not depend on any gains which can be subsequently applied to the deposited energy.

2.3.2. Measurement of the energy deposited in the gas by the alpha particles

The energy deposited (E_{dep}) by an alpha particle in the gas is the sum of the energy deposited in the drift space and the amplification space 1. E_{dep} is calculated considering both the charge deposits along the X and Y axis. Fig. 5 shows a simulated charge histogram along the X axis. This is the type of data provided by the PIM detector where the algorithm is applied.

The relationship between the deposited energy E_{dep} lost by an alpha particle to create the primary number of charges measured is given by the following equation:-

$$E_{dep} = W \times nb_{Primary\_charge} \tag{4}$$

where W (eV) is the average ionization energy (in neon gas W = 36 eV). The energy can be determined from the integral of the charge histogram (Fig. 5, right). The energy deposited in the total gas volume of the detector along the X axis (E_{depX}) is not the integral of the entire charge histogram, but only the integral of the green area (right of Fig. 5). E_{depX} can be determined using the decomposition depicted in Fig. 5 (right), following Eq. (5):-

$$E_{depX} = E_{totalX} - E_{peakX} + E_{extrapolationX} \tag{5}$$

where E_{totalX} is the integral of energy measured all along the track (in the drift space and amplification space 1), E_{peakX} the integral of energy in the amplification peak ($E_{peakX} = E_{1x} + E_{extrapolationX}$), and $E_{extrapolationX}$ is the energy corresponding to the mean of the primary charges created in the amplification space and multiplied by W. The same calculation is performed for determining E_{depY} for the charge histogram relates to the Y axis, E_{dep} being finally obtained by $E_{depX} + E_{depY}$. The charges related to E_{dep} measurement undergo several stages of amplification and drift, which degrades the resolution on the measured E_{dep}. The main charge peak cannot be used to determine E_0 because it corresponds to the energy deposited in the first amplification zone. This one undergoes a gain which is a function of the Z position of the charge created in the amplification space. During this process, the information on the deposited energy is thus degraded. As a consequence, the energy resolution would be insufficient using the main charge peak because the energy deduced from the main peak would be difficult to compare to E_{dep}.

2.3.3. Length of ionization tracks of particles in the gas, and selection of long tracks

As stipulated previously in Section 2.2.2 the calculation of track length is only possible for particles passing through the whole thickness of the detector. Nevertheless, an additional selection criterion of the tracks is necessary. Indeed, some of the preserved tracks correspond to alphas transmitted with a low angle of incidence. This implies that the deposited energy will be overlapped with the amplification peak. Moreover, a certain number of bins is necessary for the calculation of $E_{extrapolation}$. Therefore, a minimum projected track length $d_{proj} = \sqrt{dx\_min^2 + dy\_min^2}$ is required in order to correctly measure

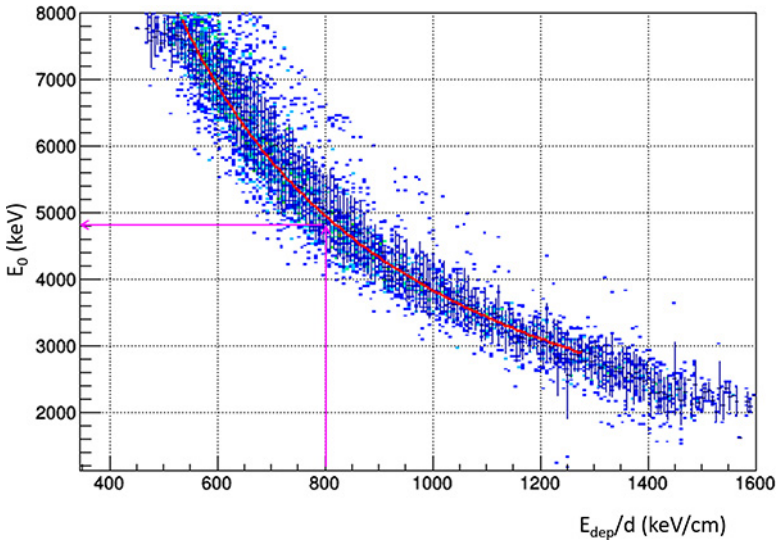

Fig. 7. Distribution of E_0 according to E_{dep}/d, obtained for particles sorted by kurtosis and projected distance criteria (Bethe curve). The distribution is adjusted by a power law (in red).

the deposited energy. This minimum length is set to d_{proj}=0.71 cm as dx_min = dy_min = 0.5 cm. (this length corresponding to 5 bins of the charge distribution in E_{peak} plus 8 bins to calculate $E_{extrapolation}$ and $E_{dep,}$ where 1 bin is equal to 400 μm). By applying this distance filtering in the *X* and *Y* axes, an overall theoretical efficiency of 5% is obtained for the spectral reconstruction. Note that this filtering also allows the elimination of a very large number of particles that do not pass through micromesh 1. Only 0.075% of these particles are selected by this distance filtering. Thus, the pollution from these particles is considered as negligible. To summarize, extracting E_{dep} from the charge histograms imposes a selection on d_{proj} in addition to the kurtosis criterion; these selections reduce the theoretical efficiency to 5%. This efficiency is the amount of alpha selected for the energy spectrum reconstruction divided by the amount of alpha reaching the detector and used to create the autoradiograph image. By calculation, 37% of the whole type-3 alphas are selected for energy reconstruction.

2.3.4. Reconstruction of the energy spectrum of the source

The energy dE lost by a particle per unit length dX in a medium is defined by the linear stopping power S = −dE/dx (MeV/cm). This can be described for a charged particle by the Bethe formula [50]. The stopping power depends on both the kinetic energy of the particle, and the transverse medium. The stopping power (or the mass stopping power $S.1/\rho$) is referenced on the ASTAR database [51] and plotted as a function of the kinetic energy for alpha particles in Supplementary Material, Figure S2. For the range of 2 MeV to 100 MeV the near-linearity of the log–log plot over S Energy suggests a power law relationship of the form $dE/dx = cE^d$ or reciprocally $E = a(dE/dx)^b$. For a non-relativistic particle, at moderate energies, the Bethe formula is dominated by $1/v^2$ or inversely with particle energy, suggesting b = 1. However, it represents only a theoretical approximation; furthermore, the Bethe formula breaks down at very low energy. So, the power function with "b" and "a" as parameters will be used in this section as a fitting function to establish the relationship between E_{dep}/d and E_0.

In addition, a gaseous detector needs amplification in order to have enough charge collected to detect a signal above the electronic noise. So, the energy deposited in the gas (E_{dep}) can be defined as an initial energy deposited in the gas (E_{dep_ini}) multiplied by a gain G_2 created by the amplification space 2:-

$$E_{dep} = G_2 \times E_{dep\_ini} \tag{6}$$

The emission energy E_0 of the particle is calculated as a function of the energy deposited in the gas (E_{dep}) and the length of the track (d) by applying a power function (Eq. (7)), which corresponds to the fit of the bijection linking E_{dep}/d and E_0 obtained on the type-3 alpha (see above Fig. 4):-

$$E_0\left(\frac{E_{dep}}{d}\right) = a \times \left(\frac{E_{dep}}{d}\right)^b \tag{7}$$

For any gain G_2, the power law for the calibration function can be written as Eq. (8):-

$$E_0\left(\frac{E_{dep}}{d}\right) = a \times \left(\frac{G_2 . E_{dep\_int}}{d}\right)^b \tag{8}$$

For a detector without gain (i.e. G_2 = 1), there is a new function with new coefficient a' and b' defined in Eq. (9).

$$E_0'\left(\frac{E_{dep\_ini}}{d}\right) = a' \times \left(\frac{E_{dep\_int}}{d}\right)^{b'} \tag{9}$$

There is an equality with energy measurement $E_0 = E_0'$, which means that (8) = (9). Theoretically, b must depend only on the physical parameters of the detector, mainly the density and the gas composition. That results in the calculation of G_2 in Eq. (10):

$$\begin{cases} b = b' \\ G_2 = \left(\frac{a'}{a}\right)^{\frac{1}{b}} \end{cases} \tag{10}$$

In order to simplify the simulation, the choice was made to fix G_2 = 1. In this case E_{dep} is equal to E_{dep_ini} and the coefficients become b = b' = b_sim, and a = a' = a_sim.

Fig. 7 illustrates the relationship between the energy deposited by the particles in the gas per unit length (E_{dep}/d) and the initial energy of the particles (E_0) more precisely. The parameters a_sim and b_sim of this power law are determined by adjustment (see red curve Fig. 7). The fit gives a_sim = 20183600 and b_sim = −1.26.

This distribution has been drawn without plotting the alpha that interact with micromesh 1 and lose part of their energy inside it. The effect of those alpha is visible on Fig. 8 where E_0_reconstructed, a function of E_0_initial, should follow a linear function if the spectral reconstruction succeeds. For 74.5% of alpha, it is the case. But for 24% the initial energy is modified. This modification is not an error of reconstruction because it is intrinsically due to interaction between the alpha and micromesh 1 (alpha can be of type-2 or -3). However, the selected alpha with E_0 < 1.5 MeV (1.5%) do not follow the power

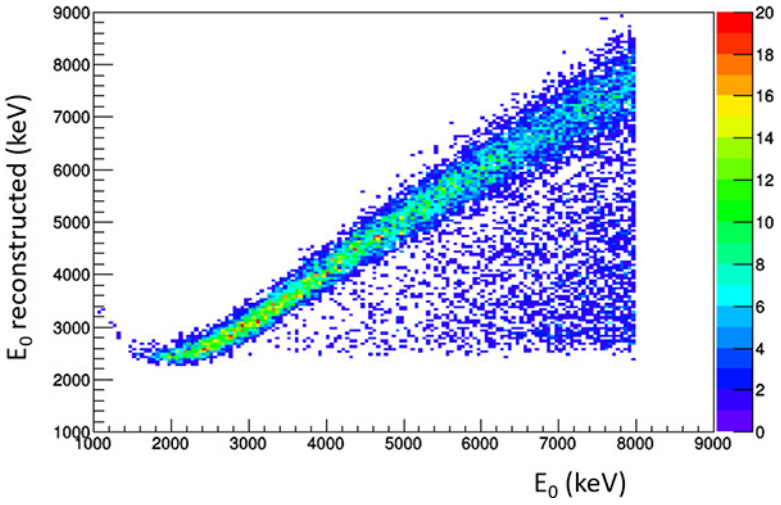

Fig. 8. Distribution of E_0 reconstructed versus E_0 initial when the particle leaves the source.

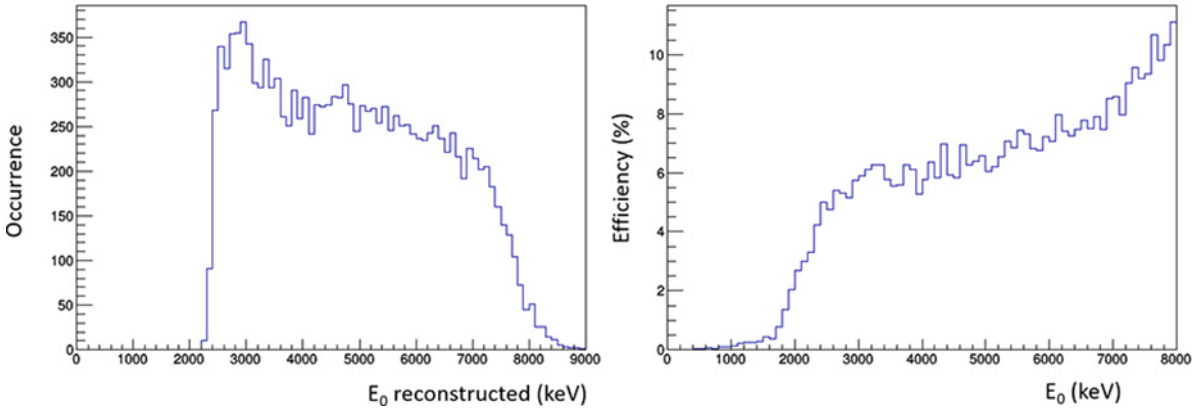

Fig. 9. Left: Reconstructed spectrum, obtained from a uniform activity source; Right: efficiency of the reconstruction method.

reconstruction function precisely. Those effects are visible in the final energy spectrum reconstruction on Fig. 9.

Fig. 9 (left) gives the initial energy spectrum E_0 obtained with the algorithm described in this section, which would have been a uniform spectrum between 0 MeV and 8 MeV. The corresponding efficiency Fig. 9 (right) is the number of alpha selected in the spectrum with original energy E_0, divided by the number of alpha generated by the source at E_0 energy.

Firstly, on the reconstructed spectrum, an under-count of around 8 MeV is observed, caused by the effect of energy resolution. Secondly, between 2 and 3 MeV, an over-count is observed, caused by: (1) calorimetric particles which are not filtered by the kurtosis criterion (with $E_0 < 1.5$ MeV) and which are reconstructed as higher energy they have; and (2) alphas which lose energy because of micromesh 1. Thirdly, another effect is visible on the reconstructed spectrum. It looks as if the spectrum decreases slightly from 4 to 8 MeV which is contradictory to the efficiency curve. This does not stem from the efficiency of the detection method. Such behaviour is inherited from the selected alpha which interact and lose energy inside micromesh 1 and change the final distribution of reconstructed energy.

As a consequence, the range of the spectrum lower than 3 MeV has not been used because of the over-count in that range. The maximum energy studied is 8 MeV (this is a limitation coming from ^{238}U series). The valid measurement ranges from 3 to 8 MeV. In this case, the mean efficiency is defined by the number of alpha falling inside this energy range [3–8 MeV] divided by the total number of alpha detected, and has a value of 3.9%.

The Geant4 simulation used in this section has its own limitations. For instance, thermodynamics phenomena (variations of temperature and pressure) are not considered, as well as electronic noise associated to the ASIC reading. Moreover, electric fields, recombination phenomena and grid transparency are not considered. The electron drift speed is not taken into account in the proposed simulations (Vd_electron = 5 cm/μs), which may induce shifts in the charge measurement between the beginning and end of the track. No physical simulation of the gain G_2 in the second amplification space (this gain is considered as unitary) has been performed. Some parameters of the simulation are defined after experimental feedback, such as the amplification gain in the first space. The proposed simulation is however sufficient to obtain data and spectra comparable to those measured by the PIM detector. By analysing these data, a methodology is established here that enables the measurement of an energy spectrum of an alpha particle source.

3. Results

The previous section described a method to theoretically measure an energy spectrum for alpha particles. In order to apply this method to real samples it is important to develop a calibration method. A calibrated sample with multiple radionuclides was used.

3.1. Thin source of ^{226}Ra used for calibration

The calibration source described (named ^{226}Ra source) is a disk (NucFilm Disc™) composed of a thin layer of manganese dioxide containing radium-226. This source covers a polyamide support of 24 mm

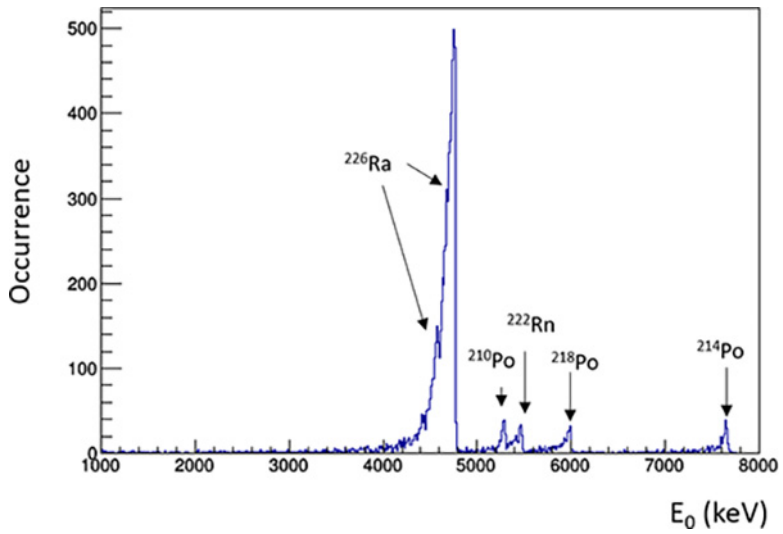

Fig. 10. Energy spectrum of the ^{226}Ra source obtained with an alpha spectrometry chain (acquisition made in 2017).

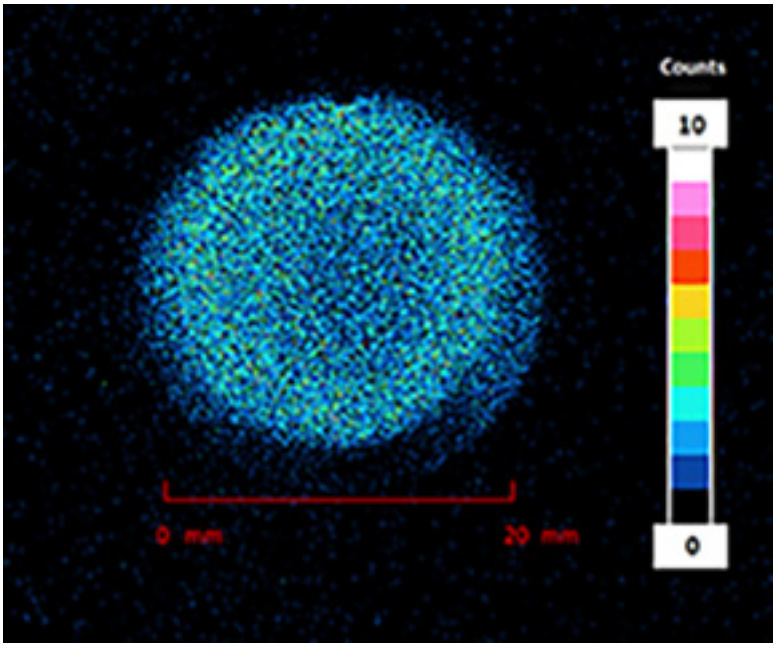

Fig. 11. Alpha autoradiograph of the ^{226}Ra source obtained with the autoradiograph. A surface counting rate of 0.32 cps was measured.

diameter. The ^{226}Ra is trapped in a 20 mm diameter area. The ^{226}Ra decays and emits an emission energy spectrum which is assimilated to that of a thin source including the ^{226}Ra and its decay products (Supplementary Material, Table S1).

In Fig. 10 the spectrum of the ^{226}Ra source was measured using an alpha spectrometer CANBERRA model 7401, coupled with a passivated implanted planar silicon (PIPS) detector for alpha spectroscopy (A450-18AM, 450 mm^2, 18 keV FWHM at 5.486 MeV). The ^{226}Ra activity is higher than for its daughters. For an acquisition time of 28811 s (~8 h), the recorded counting rate is 0.28 cps for an energy spectrum ranging from 1 to 8 MeV. The alpha spectrum is not that of a perfectly fine source, but it comes close. For the presented application, this source is nevertheless considered as a fine source because the width of the observed peaks is well below the energy resolution of the used device.

The measurement was conducted using a large area sample holder (12 × 8 cm^2) with the BeaQuant, using Alpha-mode, with the ^{226}Ra source in the center of the sample holder. This sample holder was a little different from the configuration used in the simulation. In this case, the source needed to be placed on another micromesh. Each contact between this micromesh and the source reduced the number of alpha detected, and introduced an optical transparency of 51%. But this new component did not change the methodology used for the energy measurement. The autoradiograph representing the spatial distribution of the radioactivity on the source surface is shown in Fig. 11.

To determine the a and b parameters of Eq. (7), it was necessary to use a calibration source during each acquisition. This source had to contain two sufficiently distinct energy peaks E_{cal1} and E_{cal2}, separated by at least 2 MeV, in a range between 3.5 and 8 MeV; the ^{226}Ra source with its daughters was then used as a calibration source. Its emission spectrum contains the main ^{226}Ra peak at 4784 keV and the ^{214}Po peak at 7686 keV. In this sample, the system of two equations with two unknowns to be solved is the following (Eq. (11)):-

$$\begin{cases} a \times x_1^b = E_{cal1} \\ a \times x_2^b = E_{cal2} \end{cases} \tag{11}$$

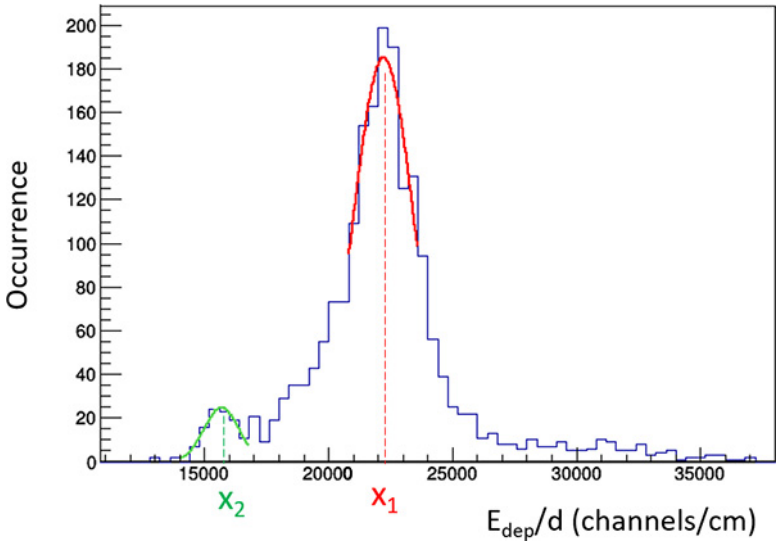

Fig. 12. Distribution of E_{dep}/d for selected alpha particles of ^{226}Ra calibration sample.

where x_1 and x_2 are the values of E_{dep}/d associated respectively with E_{cal1} = 4670 keV and E_{cal2} = 7392 keV. These values are calculated by fitting the degraded alpha energy spectrum of Fig. 10, to take the detector energy resolution into account. This degraded alpha energy spectrum is obtained by convolving the spectrum on Fig. 10 by a normal law of fixed standard deviation (σ = 342 keV). Because the energy resolution is "worth" more than the energy resolution of the spectrum on Fig. 10, the two energy peaks E_{cal1} and E_{cal2} do not correspond to the peaks defined above. An average of energy around the two peaks results from this degradation, which is however very close to their theoretical values. Moreover, the corresponding theoretical energy is also shifted by the sample thickness.

The expression of a and b is deduced by Eq. (12):-

$$\begin{cases} b = \dfrac{\ln\left(\frac{E_{cal1}}{E_{cal2}}\right)}{\ln\left(\frac{x_1}{x_2}\right)} \\ a = \sqrt{E_{cal1} \times E_{cal2}} \times e^{-b\ln\left(\sqrt{x_1 x_2}\right)} \end{cases} \tag{12}$$

To determine the variables X_1 and X_2, a fitting of the E_{dep}/d distribution (Fig. 12) is performed using two Gaussian functions. These histograms were built after selecting particles passing through the detector according to the method described in Section 2.3. The values of X_1 and X_2 correspond to the expectation of each normal distribution. In the example of the ^{226}Ra source studied, X_1 = 22220 channels/cm and X_2 = 15686 channels/cm.

The calibrated values of the coefficients calculated using Eq. (12) are $b = -1.31$ and $a = 2422661904$. It can be seen that a and b are different from the simulation (a_sim and b_sim), and this shows the need for a calibration.

Finally, the energy E_0 is measured particle by particle with the power law defined with the parameters a and b calculated previously. Fig. 13 shows the spectrum reconstructed with this power law. The spectrum is plotted on Fig. 13 (in red) and superimposed on the alpha spectrum obtained with alpha spectrometry after degradation. It is consistent with the spectrum of the source measured by alpha spectrometry and confirmed the hypothesis that the proportion of ^{226}Ra has remained constant over time. The energy resolution of the PIM detector can also be deduced from these results. It is measured at 7.3% (K = 1) or 17.2% FWHM at 4647 keV by fitting the corresponding peak with a normal distribution. The corresponding reconstruction efficiency is 5.4% between 3 and 8 MeV.

The coefficient "a" depends on the gain G_2 corresponding to the second amplification space. This gain G_2 is a constant multiplication factor applied to E_{dep} for all alpha events and can vary from one acquisition to another. The method to determinate the coefficient "a" (or indirectly G_2) is described in the next section.

3.2. Calibration optimization when the gain G_2 is variable

It can be seen that the "a" coefficient from the calibration method is far higher than from the simulation "a_sim". Such a result is in agreement with the expression of the "a" coefficient, including the gain G_2. Eq. (13) gives the relation linking G_2 and "a" coefficient:-

$$\begin{cases} b = b' \\ a = \dfrac{a'}{G_2^b} \end{cases} \tag{13}$$

where a' and b' are coefficients from a real acquisition using gain G_2 = 1, and a and b are coefficients from a real acquisition with any gain G_2 (because $b < 0$ and $G_2 > 0$ then $a > a'$).

It can be seen that G_2 is easier to introduce because it gives a physical sense to the "a" coefficient. G_2 can be determined thanks to the calibration process described hereafter.

Concurrently, the coefficients a' and b' cannot be determined experimentally because if we set G_2 = 1 with the electronics, there will not be enough charge collected by the detector to go above the threshold charge detection. However, the modelling described in Section 2.3 was achieved with G_2 = 1 ($E_{dep} = E_{dep\_int}$). So, it is possible to fix the coefficient by a' = a_sim. Another issue is that b' = b ≠ b_sim. So, if a_sim is used, the results of G_2 will not be the realistic value of the gain, but a relative value (because a_sim is an approximation of a'):-

$$G_2 = \left(\frac{a\_sim}{a}\right)^{\frac{1}{b}} \tag{14}$$

According to this method the value of G_2 can be estimated with Eq. (14). With the calibration source a calculated value is $G_{2\_cal} = 38.16$.

Now, the calibration processes can be optimized in order to calibrate "any" sample by calculating the "a" coefficient. For that, the coefficient b = −1.31 is fixed by the calibration method thanks to the ^{226}Ra source. Then, the coefficient a'= a_sim = 20183600 is also fixed. Finally, G_2 is calculated when the difference ε (defined in Eq. (15)) between the spectroscopy chain alpha spectrum distribution after degradation ($S1_i$) and the spectrum distribution ($S2_i$) is a minimum. G_2 can be "adjusted" (so "a" also changes). ε is plotted in Fig. 14 for different value of G_2.

$$\varepsilon(G_2) = \sqrt{\sum_{i=1}^{n}(S1_i - S2_i(G_2))^2} \tag{15}$$

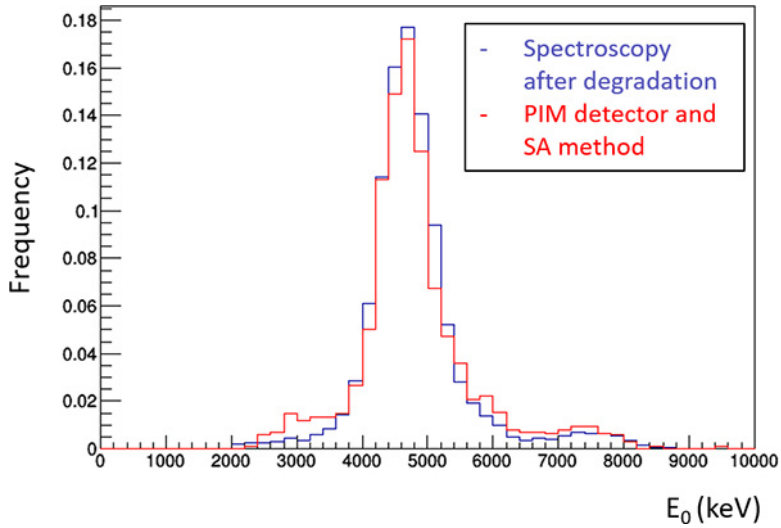

Fig. 13. Comparison of the spectrum (divided by their respective integrals) of the calibration source (^{226}Ra) obtained experimentally with the PIM detector and SA method (red) with the spectrum obtained from the spectroscopy chain, after degradation (blue).

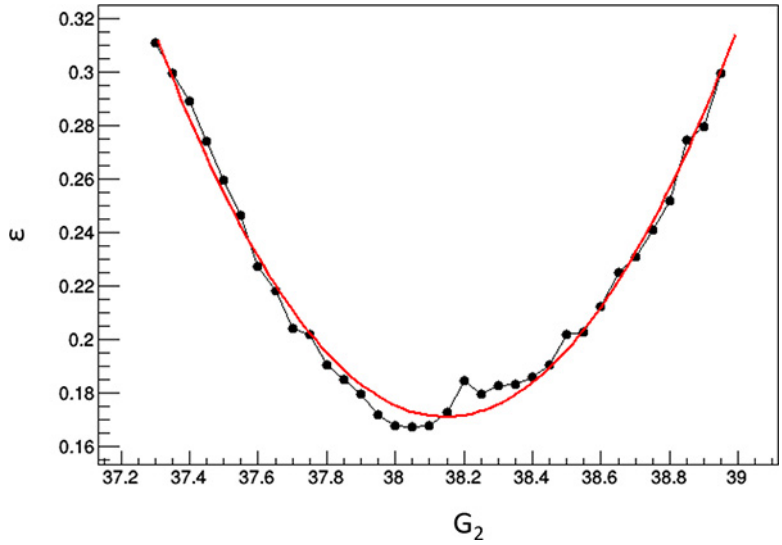

Fig. 14. Difference between spectrum 1 (spectroscopy chain alpha spectrum distribution after degradation) and spectrum 2 (PIM detector spectrum depending of G_2) distributions for ^{226}Ra source, function of gain G_2.

By applying this minimization of error technique, a corresponding $G_2 = 38.15$ was determined when ε is at its minimum. G_2 is nearly identical to G_{2_cal} with the first calibration process. With this technique, any sample can be calibrated if the alpha spectrum determined by alpha spectrometry is known.

3.3. Application using a geological sample

In order to test and validate the energy spectrum reconstruction method, an acquisition of a thick geological sample exhibiting ^{238}U and its decay products at secular equilibrium was achieved. The results are described hereafter.

The source is a uranium ore from Congo (rock age 600 My), containing uraninite (UO_2), and showing some localized uranotile and coffinite alterations. It was prepared at Bessines sur Gartempe (France) and comes from the historical collection of Orano Mining (sample 9689–03). The sample is in the form of a 7 mm-thick uraninite "piece" placed in a resin and polished on its surface. The emission energy spectrum of this source was measured with an alpha spectrometer CANBERRA model 7401 (Fig. 15), over an acquisition time of 9671 s (~2.5 h). The measured counting rate is 83.7 cps between 3000 keV and 8000 keV.

The sample is considered as a multi-alpha thick source. The measured spectrum corresponds to the superposition of eight energy steps coming from the eight alpha emitters of the ^{238}U natural decay chain (Supplementary Material, table S2). The source is at secular equilibrium, so that all isotopes from the decay chain demonstrate the same alpha activity. In the ^{238}U series, 2.5 My are approximately necessary to reach secular equilibrium (corresponding to about ten periods of ^{234}U).

The autoradiograph image shown in Fig. 16 (right) was performed with the large area sample holder in order to be under the same conditions as the calibration source presented above in Alpha-mode. The surface activity measured is 418 cps (or 0.9 cps/mm^2). The acquisition time used for measuring a spectrum on the whole section is 7239 s.

The spectrum of the ^{238}U sample is measured by applying the spectral reconstruction method. This spectrum is shown in red in Fig. 17, and it was adjusted using the calibration method described in Section 3.2, with the error ε minimization. During this calibration, the spectrum taken as a reference for the calculation of error is the one

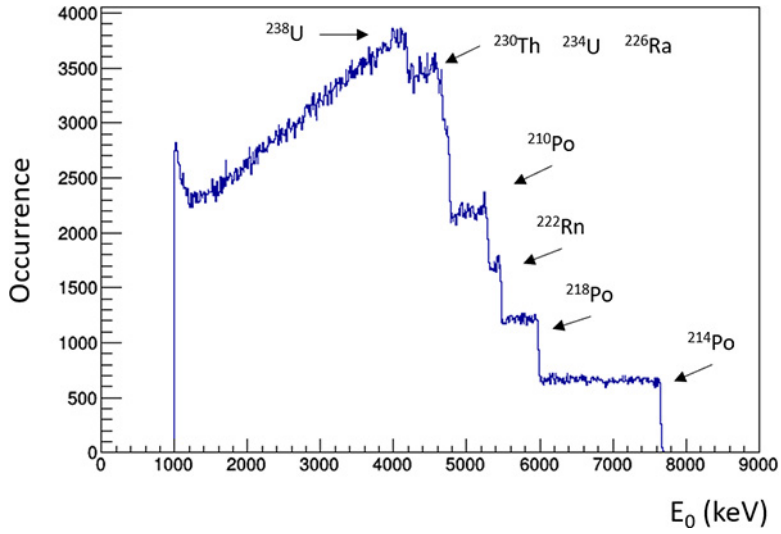

Fig. 15. Energy spectrum of uranium ore sample measured by alpha spectrometry. There are 8 alpha emitters from the ^{238}U decay product: ^{238}U, ^{234}U, ^{230}Th, ^{226}Ra, ^{222}Rn, ^{218}Po, ^{214}Po and ^{210}Po.

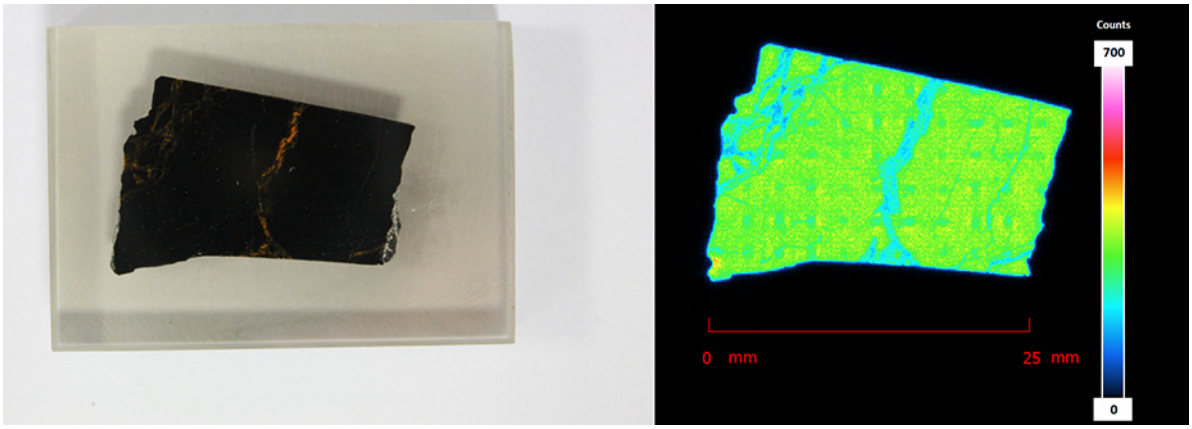

Fig. 16. Picture (left) of the uranium ore sample from the Congo (in the form of a "piece") and the corresponding alpha autoradiograph (right).

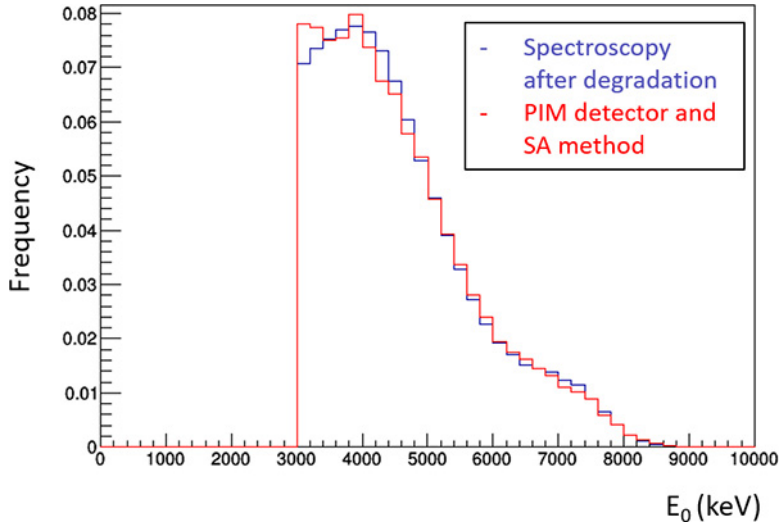

Fig. 17. Comparison of the spectrum (divided by its respective integrals) of uranium ore obtained with the PIM detector and SA method (in red) with the spectrum obtained from the spectrometry chain after degradation (in blue).

from Fig. 15 which has been degraded by normal function convolution (shown in blue on Fig. 17). The calibration leads to the calculation of gain $G_2 = 36.90$. The spectrum matches the alpha spectroscopy chain. The counting rate recorded in the range of [3–9] MeV is 18.7 cps. So, the efficiency of the spectrum reconstruction is 4.4% in this energy range, and the PIM detector has 22.3% of the efficiency of the alpha spectrometer described above. The superposition region around 3 MeV is still visible. A slight decrease in efficiency at 4.5 MeV is also observed. Overall, the two spectra in Fig. 17 are very similar.

The results mean that the PIM detector can both measure the position of alpha particles and measure their energy. The efficiency of the developed spectroscopic technique is globally low. This can be a detection limit for some applications if the sample activity is low. The acquisition time can also be adjusted to compensate with this low efficiency. For example, considering that 2000 entries in the energy spectrum are sufficient for interpretation, this corresponds to a count rate of 0.075 cps for one week of acquisition time. In terms of uranium content, and considering a 1 mm^2 region of interest, this count rate is related to about 3 wt% of uranium in secular equilibrium. If the application of the spectral modality seems feasible for multi-source, it needs to be tested more deeply for heterogeneous geological samples.

4. Conclusion

The described energy spectrum measurement method is based on an algorithm applied to data of an ideal point source representing the interaction of alpha particles with a PIM detector, whose elements were geometrically optimized. The spectral reconstruction efficiency is 4.4%, and the energy resolution is poor compared to a semiconductor (but is still better than other technologies). In addition, the efficiency can surely be improved by using a sample holder in exactly the same configuration as shown in Fig. 1, and also by optimizing the algorithm of energy reconstruction. However, these results already make it viable to use spectroscopic autoradiography on geological samples. This measurement will allow the study of the spatial distribution of uranium and its descendants in geo-materials by coupling SEM characterizations. For this purpose, a complementary complex radioactive source material modelling could be considered. The direct application of this dual modality (energy-position) of analysis will be the subject of future developments. The measurement of the radioactive equilibrium state of heterogeneous geological structures, and the quantitative mapping of ^{226}Ra radioactivity are now being actively studied.

Declaration of competing interest

The authors declare the following financial interests/personal relationships which may be considered as potential competing interests: This research work is performed by a collaboration which includes three private companies which are respectively ORANO, ERM Poitiers and ai4r. In this context, Hugo Lefeuvre reports financial support provided by ORANO, ai4r and ERM.

Acknowledgements

This work has been done within the framework of a CIFRE Ph.D. thesis (n° 2020/0166) convention between the University of Poitiers, ERM (SARL) (Poitiers, France) and ANRT. We would like to thank Marc Brouand (ORANO Mining company) for the samples preparation. We would like to thank Julie Champion from Subatech Laboratory for her valuable assistance during the spectroscopy measuring campaign.

Appendix A. Supplementary data

Supplementary material related to this article can be found online at https://doi.org/10.1016/j.nima.2022.166807.

References

[1] F. Bourrel, P. Courrière, Radionucléides - application : biologie moléculaire, in: Techniques de L'Ingénieur, Vol. V1, 2003, pp. 3362–3363.
[2] P. Fichet, et al., Tritium analysis in building dismantling process using digital autoradiography, J. Radioanal. Nucl. Chem. 291 (2012) 869–875.
[3] G.A. Boyd, Autoradiography in Biology and Medicine, Academic Press, 1955.
[4] A. Biegon, C. Mathis, W. Jagust, Autoradiography As a Tool for PET/SPECT Tracer Selection and Assessment, Academic Press, 1996, pp. 26–33.
[5] O. Alitalo, et al., Digital autoradiography for efficient functional imaging without anesthesia in experimental animals: Reversing phencyclidine-induced functional alterations using clozapine, Progr. Neuro Psychopharmacol. Biol. Psychiatry 100 (2020) 109887.
[6] E. Muuri, et al., Electronic autoradiography of ^{133}Ba particle emissions; diffusion profiles in granitic rocks, Appl. Radiat. Isot. 149 (2019) 108–113.
[7] N. Macé, P. Fichet, et al., Use of quantitative digital autoradiography technique to investigate the chlorine-36-labelled radiotracer transport in concrete, Appl. Geochem. 100 (2019) 326–334.
[8] M. Voutilainen, et al., Characterization of spatial porosity and mineral distribution of crystalline rock using X-ray micro computed tomography, C-14-PMMA autoradiography and scanning electron microscopy, Appl. Geochem. 101 (2019) 50–61.
[9] G. Devès, et al., Chemical element imaging for speleothem geochemistry: Application to a uranium-bearing corallite with aragonite diagenesis to opal (Eastern Siberia, Russia), Chem. Geol. (2012) 190–202.
[10] S.M. Zhmodik, et al., The study of distribution and forms of uranium occurrences in lake baikal sediments by the SSNTD method, Radiat. Meas. 4294–295 (2005) 532–538.
[11] A.A. Ochmann, A.T. Solecki, CR-39 autoradiographic micromapping of rock sections of various alpha emitters content – calibration approach, J. Environ. Radioact. 79 (2005) 127–136.
[12] T. Pi, et al., Autoradiography of Geological Fluorite Samples for Determination of Uranium and Thorium Distribution Using Nuclear Track Methodology, Vol. 53, 2007, pp. 57–60, Sociedad Mexicana de Física.
[13] S. Kodaira, et al., Evidence of local concentration of α-particles from ^{211}At-labeled antibodies in liver metastasis tissue, J. Nucl. Med. 60 (2019) 497–501.
[14] J.M. Cole, et al., Phosphor imaging as a tool for in situ mapping of ppm levels of uranium and thorium in rocks and minerals, Chem. Geol. 193 (2013) 127–136.
[15] T. Bäck, L. Jacobsson, The α-camera: A quantitative digital autoradiography technique using a charge-coupled device for ex vivo high-resolution bioimaging of α-particles, J. Nucl. Med. 51 (2010) 1616–1623.
[16] N. Chouin, et al., Ex vivo activity quantification in micrometastases at the cellular scale using the α-camera technique, J. Nucl. Med. 54 (2013) 1347–1353.
[17] B.W. Miller, Radiation imagers for quantitative, single-particle digital autoradiography of alpha- and beta-particle emitters, Semin. Nucl. Med. 48 (2018) 367–376.
[18] B.W. Miller, et al., Quantitative single-particle digital autoradiography with α-particle emitters for targeted radionuclide therapy using the iQID camera, Med. Phys. 42 (2015) 4094–4105.
[19] L. Han, B.W. Miller, et al., Applications of iQID cameras, in: Proceedings SPIE Volume 10393, Radiation Detectors in Medicine, Industry, and National Security XVIII, 2017, pp. 165–170.
[20] R.A.L. Darwish, et al., Autoradiography imaging in targeted alpha therapy with timepix detector, Comput. Math. Methods Med. (2015) e612580.
[21] C. Teyssier, et al., Exploitation of the charge sharing effect in timepix device to achieve sub-pixel resolution in imaging applications with alpha particles, in: Astroparticle, Particle, Space Physics and Detectors for Physics Applications. Vol. 7, 2012, pp. 681–687.
[22] N. Benabdallah, et al., Radium-223 treated primary patient bone biopsy analysis: Macro to microscale analyses and dosimetry, J. Nucl. Med. 61 (2020) 531.
[23] N. Benabdallah, Optimisation de la Dosimétrie En Alphathérapie Par Approche Multi-échelle : Application Au Traitement Des Métastases Osseuses Par Le^{223}Ra PhD manuscript, Université Paris-Saclay, 2017.
[24] P. Sardini, et al., Quantitative autoradiography of alpha particle emission in geo-materials using the beaver™ system, Nucl. Instrum. Methods Phys. Res. A 833 (2016) 15–22.
[25] J. Donnard, et al., Advancements of labelled radio-pharmaceutics imaging with the PIM-MPGD, J. Instrum. 4 (2009) P11022.
[26] J. Donnard, et al., The micro-pattern gas detector PIM: A multi-modality solution for novel investigations in functional imaging, Nucl. Instrum. Methods Phys. Res. A 610 (2009) 158–160.
[27] J. Donnard, et al., High spatial resolution in β-imaging with a PIM device, IEEE Trans. Nucl. Sci. 56 (2009) 197–200.
[28] S. Billon, P. Sardini, et al., From Bq cm^{-3} to Bq cm^{-2} (and conversely) – Part 1: a useful conversion for autoradiography, J. Radioanal. Nucl. Chem. 320 (2019) 643–654.
[29] S.M.H. Pooya, et al., Passive α-particles spectrometry by polycarbonate SSNTD using new etching conditions, Radiat. Phys. Chem. 77 (2008) 949–953.
[30] M.F. Zaki, Y.H. El-Shaer, Particularization of alpha contamination using CR-39 track detectors, PRAMANA J. Phys. 69 (2007) 567–574.

[31] O.A. Bondarenko, et al., Performance of alpha particle spectroscopy using a TASTRAK^{TM} detector, Radiat. Meas. 26 (1996) 59–64.
[32] Y. Morishita, et al., Detection of alpha particle emitters originating from nuclear fuel inside reactor building of fukushima daiichi nuclear power plant, Sci. Rep. 9 (2019) 581.
[33] Y. Morishita, Development of an alpha- and beta-imaging detector using a thin-stilbene plate for radon-222 progeny measurements, Radiat. Meas. 140 (2021) 106511.
[34] M. Janik, et al., Optimization of the timepix chip to measurement of radon, thoron and their progenies, Appl. Radiat. Isot. 107 (2016) 220–224.
[35] M. Holik, et al., Alpha calibration of the timepix pixel detector exploiting energy information gained from a common electrode signal, J. Instrum. 14 (2019) C06022.
[36] C. Granja, et al., Resolving power of pixel detector timepix for wide-range electron, proton and ion detection, Nucl. Instrum. Methods Phys. Res. A 908 (2018) 60–71.
[37] J. Vallerga, et al., High-resolution UV, alpha and neutron imaging with the timepix CMOS readout, Nucl. Instrum. Methods Phys. Res. A 591 (2018) 151–154.
[38] B.W. Miller, et al., The iQID camera: An ionizing-radiation quantum imaging detector, Nucl. Instrum. Methods Phys. Res. A 767 (2014) 146–152.
[39] Y. Morishita, et al., Performance comparison of scintillators for alpha particle detectors, Nucl. Instrum. Methods Phys. Res. A 764 (2014) 383–386.
[40] Y. Morishita, et al., Flexible alpha camera for detecting plutonium contamination, Radiat. Meas. 103 (2017) 33–38.
[41] J.J.M. Kouwenberg, et al., Alpha Radiation Dosimetry Using Fluorescent Nuclear Track Detectors Radiation Measurements, Vol. 113, 2018, pp. 25–32.
[42] J.A. Bartz, et al., An imaging spectrometer based on high resolution microscopy of fluorescent aluminum oxide crystal detectors, Radiat. Meas. 56 (2013) 273–276.
[43] N. Hasebe, et al., α-Particle spectrometer based on xenon gas ionization chamber using coplanar electrodes, Nucl. Inst. Methods Phys. Res. Sect. A 925 (2019) 123–127.
[44] K. Iwasaki, et al., Development of gas ionization chambers with coplanar electrodes for alpha-ray spectrometry, in: Proceedings of International Symposium on Radiation Detectors and their Uses, JPS Conf. Proc, Vol. 11, 2016, 010003.
[45] H. Ito, et al., Development of an alpha-particle imaging detector based on a low radioactivity micro-time-projection chamber, Nucl. Instrum. Methods Phys. Res. A 953 (2020) 163050.
[46] A. Angileri, et al., Mapping ^{238}U decay chain equilibrium state in thin sections of geo-materials by digital autoradiography and microprobe analysis, Appl. Radiat. Isot. 140 (2018) 228–237.
[47] S. Billon, et al., Quantitative imaging of^{226}Ra ultratrace distribution using digital autoradiography: Case of doped celestines, J. Environ. Radioact. 217 (2020) 106211.
[48] J.-F. Moyen, et al., Multi-scale spatial distribution of K, Th and U in an Archaean potassic granite: a case study from the heerenveen batholith, barberton granite-greenstone terrain, South Africa, South Afr. J. Geol. 124 (2021) 53–86.
[49] T. Siiskonen, R. Pöllänen, Advanced simulation code for alpha spectrometry, Nucl. Instrum. Methods Phys. Res. A 550 (2005) 425–434.
[50] G.F. Knoll, Radiation Detection and Measurement, third ed., John Wiley & Sons, New Work, 2000, p. 31.
[51] ASTAR, 2022, available at https://physics.nist.gov/PhysRefData/Star/Text/ASTAR.html. (Accessed 1 January 2022).